

Fe Ultra-small particles anchored on Carbon aerogels to Enhance Oxygen Reduction Reaction in Zn-Air Battery

Jinjin Shi,^a Xinxin Shu,^b Chensheng Xiang,^c Hong Li,^a Yang Li,^a Wei Du,^d Pengfei An,^{*e} He Tian,^{*c} Jintao Zhang^{*b} and Haibing Xia^{*a}

^aState Key Laboratory of Crystal Materials, Shandong University, Jinan, 250100, P. R. China. E-mail: hbxia@sdu.edu.cn;

^bSchool of Chemistry and Chemical Engineering, Shandong University, Jinan, 250100, P. R. China. E-mail: jtzhang@sdu.edu.cn;

^cCenter of Electron Microscope, State Key Laboratory of Silicon Materials, School of Materials Science and Engineering, Zhejiang University, Hangzhou, 310027, P. R. China. E-mail: hetian@zju.edu.cn;

^dSchool of Environment and Material Engineering, Yantai University, Yantai 264005, P. R. China;

^eBeijing Synchrotron Radiation Facility, Institute of High Energy Physics, Chinese Academy of Sciences, Beijing, 100049, P. R. China. E-mail: anpf@ihep.ac.cn.

Experimental section

Materials characterization

Low-resolution transmission electron microscopy (TEM) and high-resolution TEM (HRTEM) images were investigated by a JEOL JEM- 2100F transmission electron microscope operated at an acceleration voltage of 200 kV. High-angle annular dark field-scanning transmission electron microscopy (HAADF-STEM) images and energy dispersive spectrometry (EDS) mapping images were investigated by a FEI Titan G2 80-200 ChemiSTEM electron microscope operated at 200 kV.

The X-ray diffraction (XRD) patterns of the as-prepared samples were performed on a Bruker AXSD8 advance X-ray diffractometer with Cu K α radiation source using a graphite monochromator in the 2 θ range from 10 to 80 ° with a step size of 0.04 °.

The Raman spectra of the as-prepared samples were measured by a Renishaw inVia Reflex Raman spectrometer at the excitation wavelength of 633 nm.

N₂ sorption analysis of the as-prepared samples was investigated by a Micromeritics ASAP Kubo X1000 analyzer at liquid nitrogen temperature and their surface area were then calculated by Brunauer-Emmett-Teller (BET) theory. In addition, the plots of their pore size distribution were obtained by the desorption branch of the isotherm using the Barrett-Joyner-Halenda (BJH) model.

X-ray photoelectron spectra (XPS) of the as-prepared samples were investigated by the XPS spectrometer (ESCALAB 250) with a monochromatic Al K α ($h\nu = 1486.6$ eV) X-ray radiation for excitation.

The X-ray absorption fine structure spectra (Fe K-edge) were collected at the 1W1B beamline in the Beijing Synchrotron Radiation Facility (BSRF), China. And the storage ring of the BSRF was operated at 2.5 GeV with a maximum electron current of 250 mA. The energy of the incident X-rays is in the range from 4 to 25 KeV, which is tuned by using a fixed-exit Si (111) double crystal monochromator. In addition, data collection was carried out in transmission mode by using an ionization chamber for Fe foil and Fe₂O₃ and in fluorescence mode using a Lytle detector for Fe_{Fe-O-Fe}-UP/CA

catalysts, respectively. All spectra were collected under ambient conditions.

Electrochemical Measurement.

All the electrochemical measurements were carried out on a CHI 760E electrochemical workstation (CH Instruments, Inc., Shanghai) with a standard three-electrode system in alkaline electrolyte (0.1 M KOH) at room temperature. The rotating disk electrode (RDE) measurement was achieved with a glassy carbon (GC) disk of 5 mm in diameter as working electrode, a graphite rod as the counter electrode and the Hg/Hg₂Cl₂ as reference electrode, respectively.

$$E \text{ (vs RHE)} = E \text{ (vs Hg/Hg}_2\text{Cl}_2) + (0.244 + 0.0591 \text{ pH}) \text{ V (1)}$$

Before to use, the glassy carbon electrodes with a surface area of 0.19625 cm² (GCEs) were polished with alumina powder (0.05 μm in size), followed by the washing procedure of ultrapure water and ethanol under ultrasonication. After that, these GCEs were then dried at room temperature for further use.

To prepare the uniform catalyst ink, the powder of each type of catalyst (10 mg), 800 μL of water, 140 μL of ethanol and 60 μL of Nafion (5 wt%) were mixed together by ultrasonic treatment of 30 min. Then, 15 μL of each type of the as-prepared catalyst ink was coated onto one GCE with a loading of 0.764 mg cm⁻². After that, these GCEs were then dried at room temperature. For better comparison, the commercial Pt/C catalyst (20 wt%, Johnson-Matthey) was also coated onto the GCE with a loading of 0.125 mg cm⁻² (the Pt loading is 25 μg cm⁻²).

The electrolyte has to be purged by N₂ or O₂ flow was for 30 min before each oxygen reduction reaction (ORR) test. And the electrolyte was also continuously bubbled during the tests. Both cyclic voltammetry (CV) tests and linear sweep voltammetry (LSV) tests were carried out in N₂/O₂-saturated electrolyte. And the scan rate for CV and LSV tests is 10 mV s⁻¹ and 5 mV s⁻¹, respectively.

The activities of the catalysts toward the ORR were recorded at various rotating speeds ranging from 400 to 1600 rpm. The solution ohmic drop (i.e., iR drop) was compensated. In addition, the background capacitive current was tested in the N₂-saturated electrolyte under the same potential range and scan rate conditions, which

were then corrected to obtain the net ORR current of the tested catalyst.

The electron transfer number of each catalyst was calculated according to the following Koutecky-Levich equation:

$$\frac{1}{J} = \frac{1}{J_K} + \frac{1}{J_L} = \frac{1}{B\omega^{1/2}} + \frac{1}{J_K} \quad (2)$$

where J represents the measured current density at specific potential, ω is the angular velocity applied in the test, J_K and J_L are the kinetic and diffusion limiting current densities, respectively. The constant B was calculated according to the formula:

$$B = 0.62nFC_0(D_0)^{2/3}\nu^{-1/6} \quad (3)$$

where F is the Faraday constant ($F = 96485 \text{ C mol}^{-1}$), the concentration of O_2 in electrolyte (C_0) is $1.26 \times 10^{-3} \text{ mol L}^{-1}$, the diffusion coefficient of O_2 (D_0) is $1.93 \times 10^{-5} \text{ cm}^2 \text{ s}^{-1}$, and the kinetic viscosity ν is $1.009 \times 10^{-2} \text{ cm}^2 \text{ s}^{-1}$.

The chronoamperometric responses of $\text{Fe}_{\text{Fe-O-Fe}}\text{-UP/CA}$ catalysts and the commercial Pt/C catalyst were evaluated by chronoamperometry at a potential of 0.9 V vs. RHE with a rotation speed of 1600 rpm in 150 mL O_2 -saturated 0.1 M KOH.

In addition, the accelerated durability tests (ADTs) of $\text{Fe}_{\text{Fe-O-Fe}}\text{-UP/CA}$ catalysts and the commercial Pt/C catalyst were investigated by 5000 cycling test in O_2 -saturated 0.1 M KOH solution at room temperature by applying potential cycling between 1.0 and 0.2 V vs. RHE at a scan rate of 100 mV s^{-1} . The methanol crossover effect tests of $\text{Fe}_{\text{Fe-O-Fe}}\text{-UP/CA}$ catalysts and the commercial Pt/C catalyst were investigated by chronoamperometric measurement with an addition of 3 M methanol.

To assemble a primary Zinc-Air battery, 6.0 M KOH solution containing 0.2 M zinc acetate was used as the electrolyte and a zinc plate served as the anode. The air cathode was prepared by loading the corresponding catalyst ink onto carbon paper with a mass loading of 1 mg cm^{-2} , followed by drying at room temperature.

Fig. S1 TEM image of 40 nm ZIF particles without any treatment.

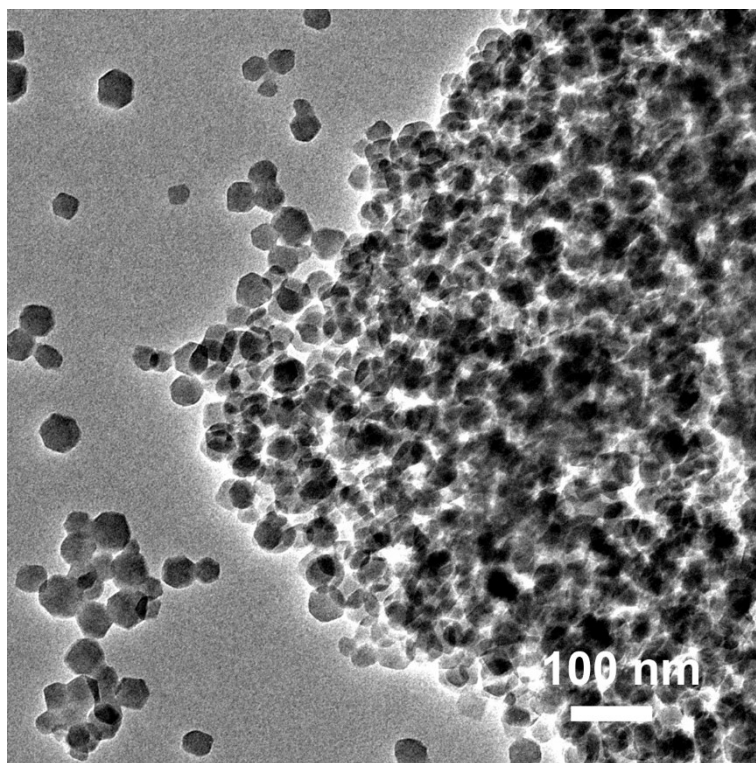
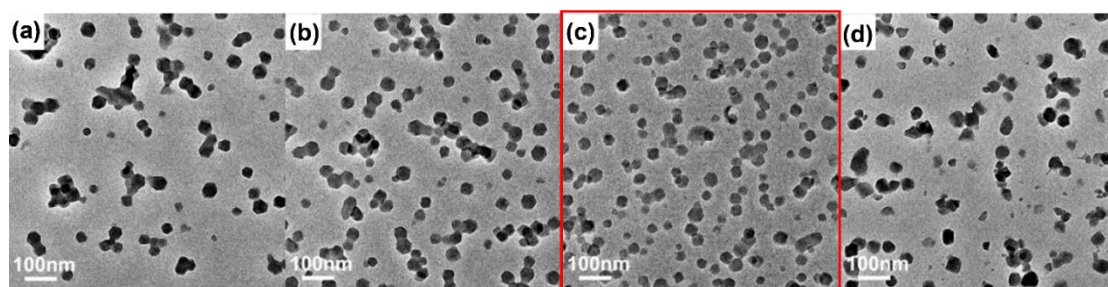
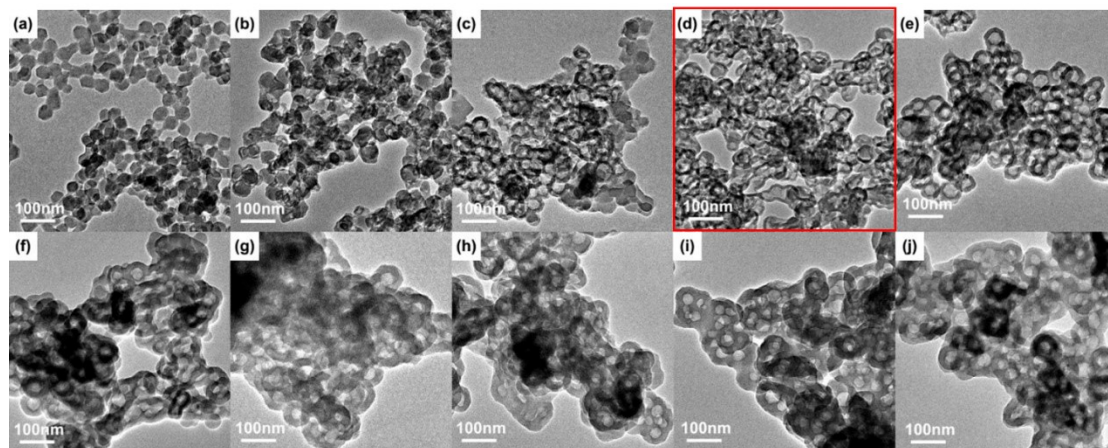


Fig. S2 TEM images of 40 nm ZIF particles after the ultrasonication treatment under different times: (a) 6 min; (b) 15 min; (c) 30 min and (d) 60 min.



According to TEM results, the optimal time of the ultrasonication treatment is determined to be 30 min.

Fig. S3 TEM images of hollow ZIF-TA particles obtained by TA-etching process at different TA concentrations: (a) 0.3 g L⁻¹; (b) 3 g L⁻¹; (c) 4 g L⁻¹; (d) 5 g L⁻¹; (e) 6 g L⁻¹; (f) 8 g L⁻¹; (g) 10 g L⁻¹; (h) 12 g L⁻¹; (i) 15 g L⁻¹; (j) 20 g L⁻¹.



According to TEM results, the optimal concentration of TA used for TA-etching process is determined to be 5 g L⁻¹.

Fig. S4 TEM images of (a) ZIF particles; (b) hollow ZIF-TA particles by TA etching (in methanol); (c) ZIF-TA-Fe particles (in water); (d) ZIF-TA-Fe after freeze-drying (powders).

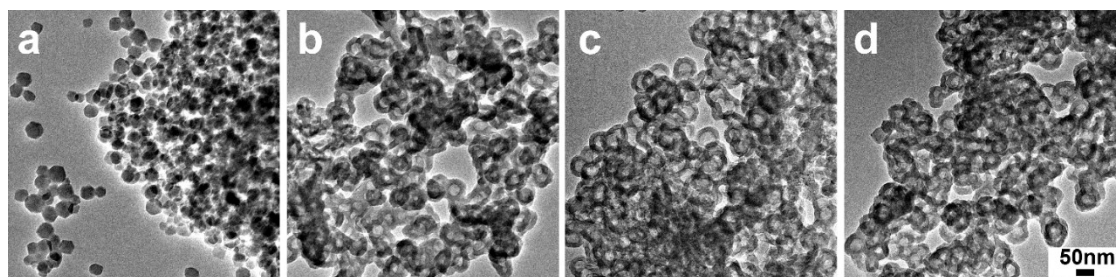


Fig. S5 XRD patterns of the ZIF particles, hollow ZIF-TA particles, and hollow ZIF-TA-Fe particles.

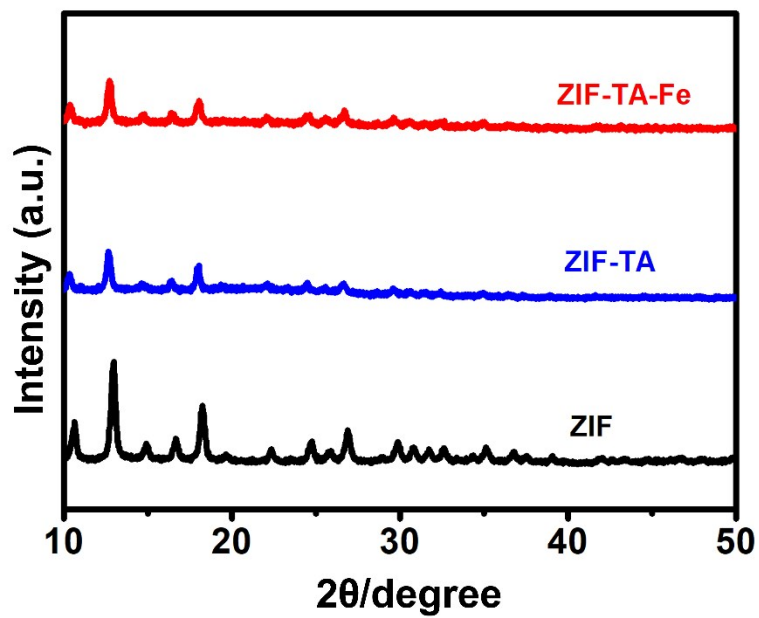


Fig. S6 Digital photograph of $\text{Fe}_{\text{Fe-O-Fe}}$ -UP/CA catalysts.



Fig. S7 Low magnification TEM images of (a) Fe-SA/CA catalysts; (b) Fe_{Fe-O-Fe}-UP/CA catalysts and (c) Fe-NP/CA catalysts. Insets are their corresponding high magnification TEM images.

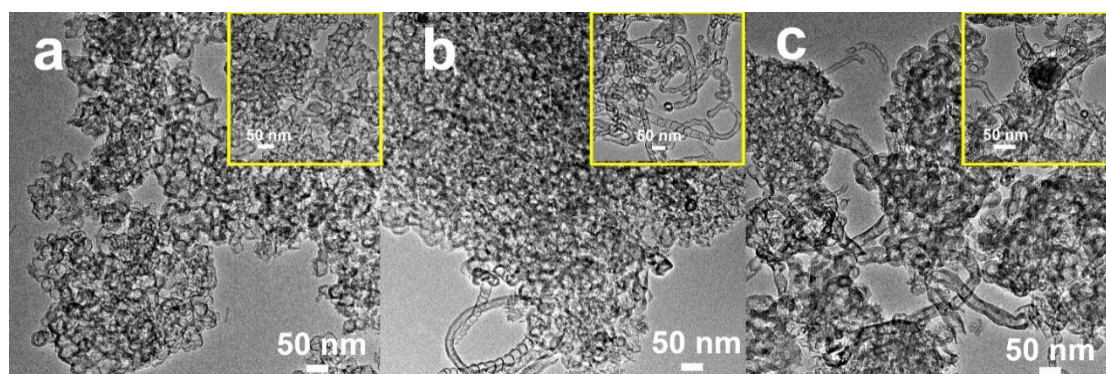
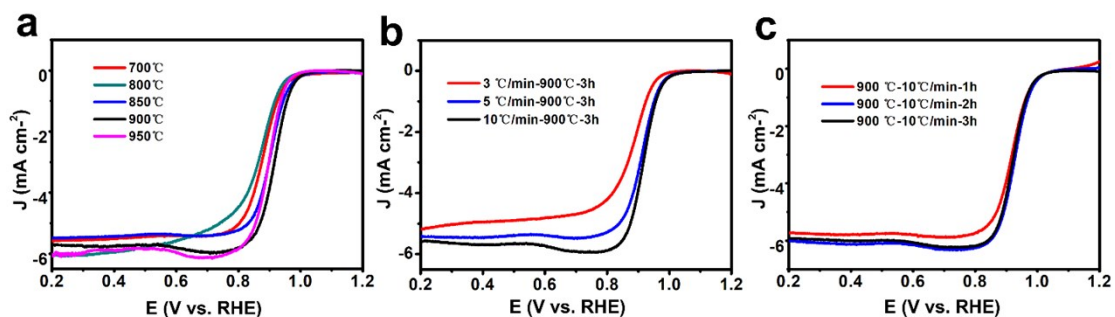
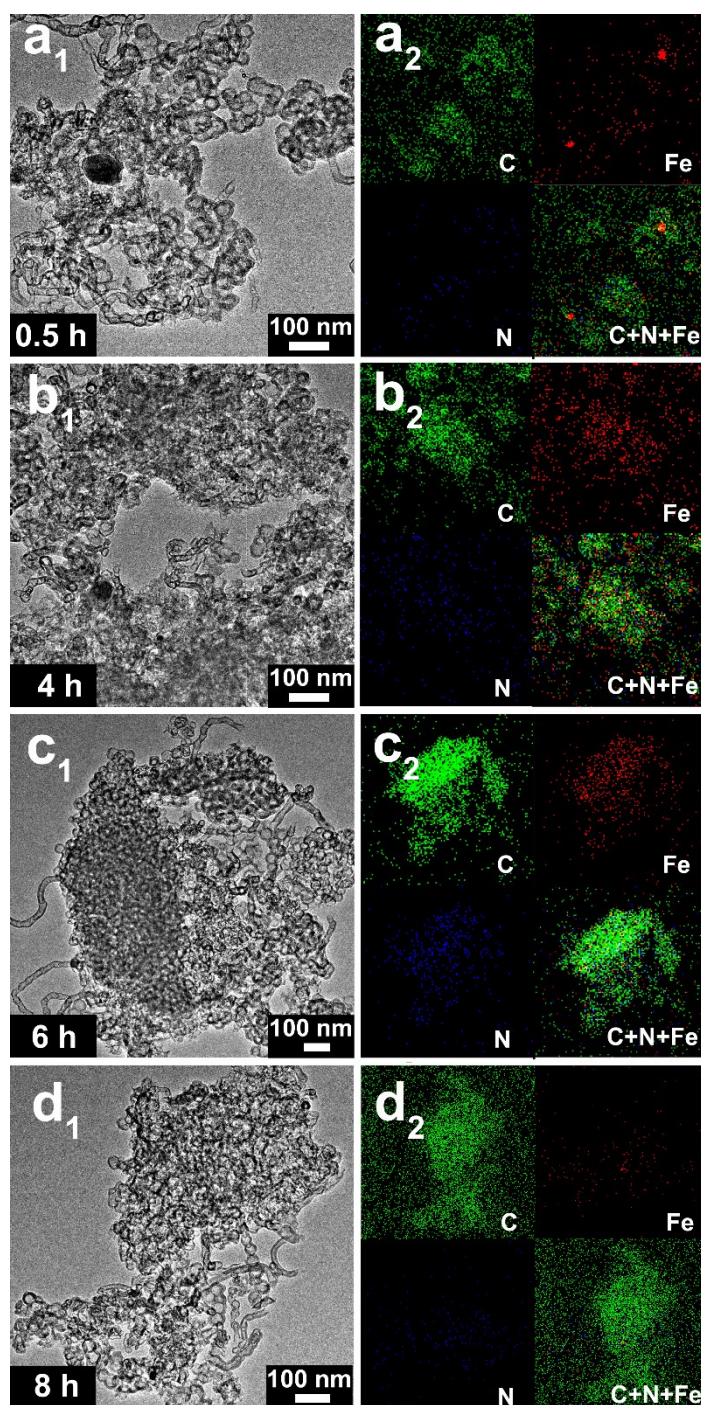


Fig. S8 LSV curves of Fe_{Fe-O-Fe}-UP/CA catalysts prepared under different pyrolysis temperatures (a), holding times (b) and hating rates (c). All of these LSV curves were measured in 0.1M KOH.



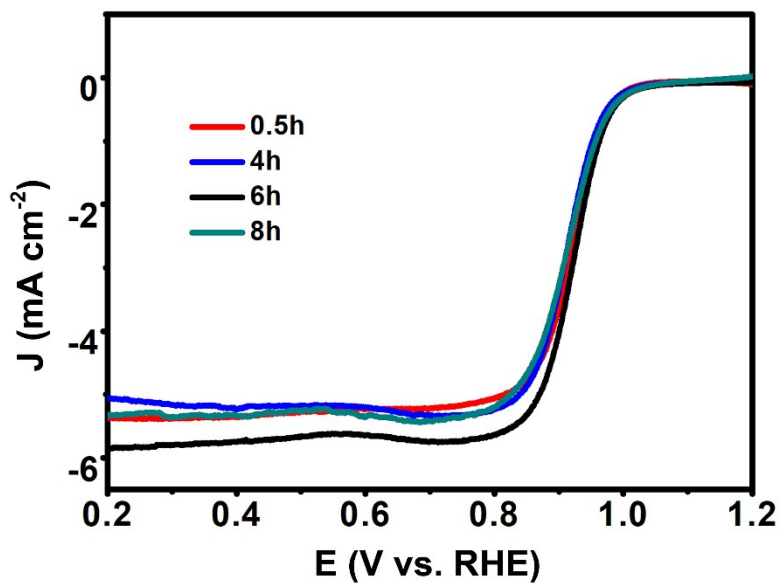
According to these LSV measurement (Fig. S8), the optimal pyrolysis condition of Fe_{Fe-O-Fe}-UP/CA catalysts is determined to be 900 °C for 3 h with a heating rate of 10 °C min⁻¹ under flowing Ar gas.

Fig. S9 TEM images and the corresponding mapping results of Fe_{Fe-O-Fe}-UP/CA catalysts after the acid leaching treatment of different times: (a₁, a₂) 0.5 h, (b₁, b₂) 4 h, (c₁, c₂) 6 h, and (d₁, d₂) 8h.



The unstable and large-sized Fe NPs in the Fe_{Fe-O-Fe}-UP/CA catalysts were almost removed (as shown in Fig. S9) after the acid treatment of 6 hours.

Fig. S10 LSV curves of Fe_{Fe-O-Fe}-UP/CA catalysts after the acid treatment of different times.



As shown in Fig. S10, the Fe_{Fe-O-Fe}-UP/CA catalysts after the acid treatment of 6 hours has the most positive half-wave potential.

Fig. S11 XRD patterns of Fe_{Fe-O-Fe}-UP/CA catalysts before and after the acid leaching treatment.

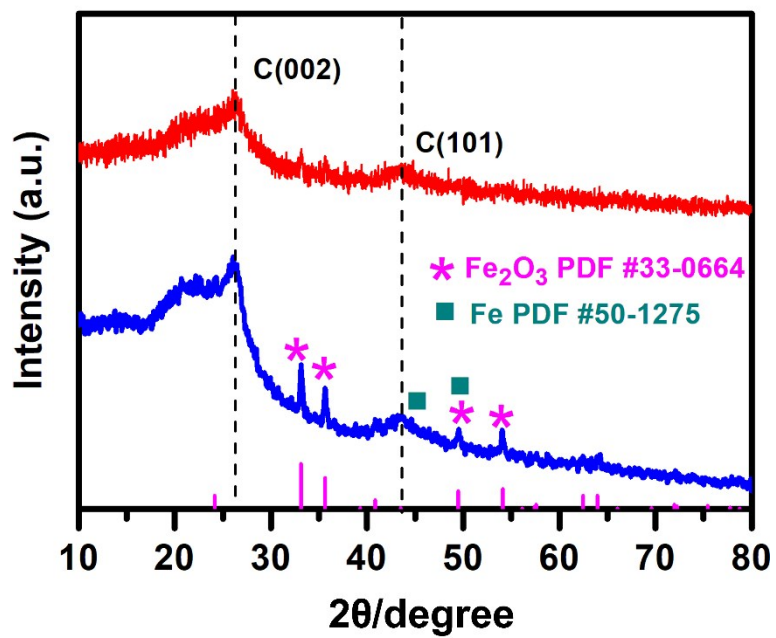
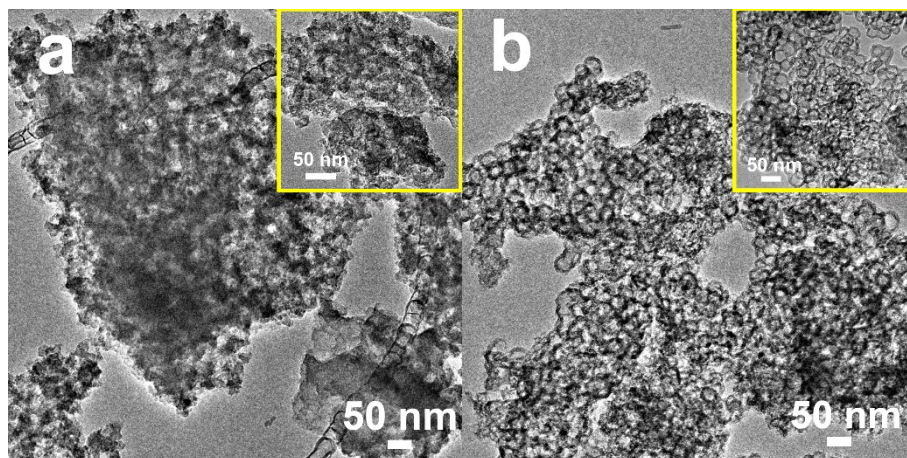


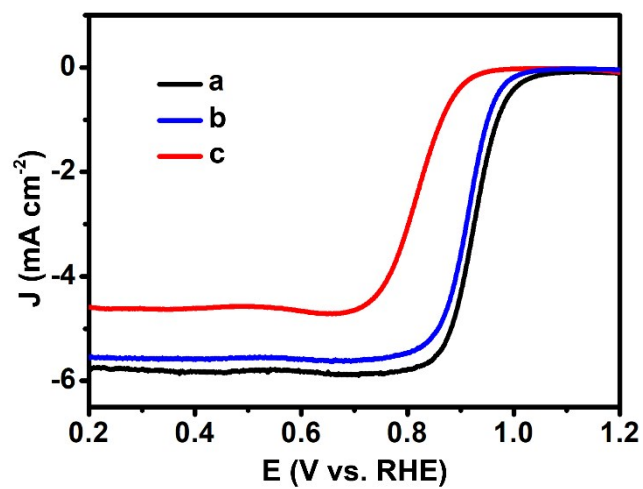
Fig. S12 TEM images of carbon materials prepared under different recipes: (a) ZIF particles with Fe precursors ($C_{\text{ZIF-Fe}}$ catalysts), and (b) hollow ZIF particles with TA ($C_{\text{ZIF-TA}}$ catalysts). Note that the amounts of Fe precursors or TA used are the same as those used for synthesis of Fe-UP/CA catalysts.



As shown in Fig. S12a, the $C_{\text{ZIF-Fe}}$ catalysts are mainly composed of aggregates of inter-connected carbon particles. In addition, a small ratio of carbon nanotubes is also existed in the $C_{\text{ZIF-Fe}}$ catalysts, which is attributed to the presence of Fe precursors.

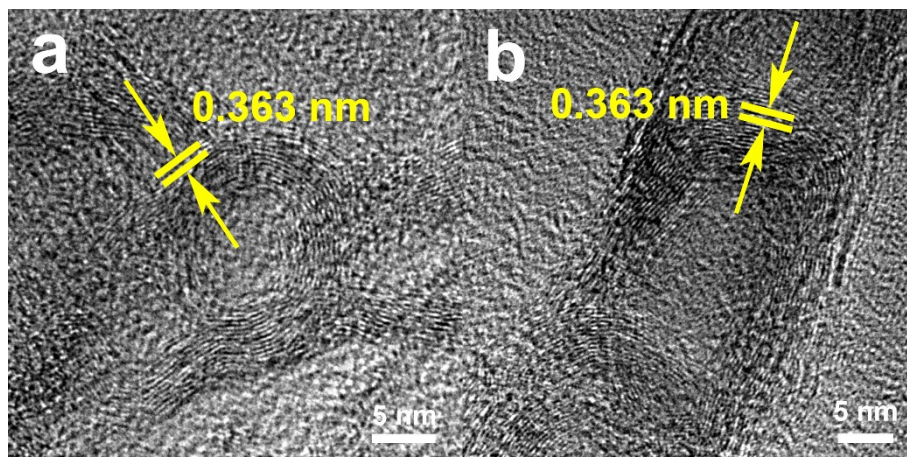
In contrast, as shown in Fig. S12b, $C_{\text{ZIF-TA}}$ catalysts are mainly composed of aggregates of hollow carbon spheres. It seems that these hollow carbon spheres are interconnected together.

Fig. S13 LSV curves of the Fe_{Fe-O-Fe}-UP/CA catalysts (a), C_{ZIF-Fe} catalysts (b), and C_{ZIF-TA} catalysts (c).



One can see from Fig. S13 that the Fe_{Fe-O-Fe}-UP/CA catalysts show a much higher half-wave potential than C_{ZIF-TA} catalysts and C_{ZIF-Fe} catalysts.

Fig. S14 High-resolution TEM images of (a) one whole carbon sphere and (b) one part of one carbon nanotube in $\text{Fe}_{\text{Fe-O-Fe}}\text{-UP/CA}$ catalysts.



High-resolution TEM images of one whole carbon sphere and (b) one part of one carbon nanotube in $\text{Fe}_{\text{Fe-O-Fe}}\text{-UP/CA}$ catalysts are shown in Fig. S14a and Fig. S14b, respectively. It can be clearly seen that the carbon sphere is indeed hollow, and its shell is composed of a few graphite-like layers that is ascribed to the (002) plane of graphitic carbon. In addition, it seems that carbon nanotubes in Fe-UP/CA catalysts are composed of interconnected hollow sphere in a head-to-tail way. Both of them show clear lattice fringes, indicating the high crystallization degree of the as-prepared CAs obtained by the pyrolysis treatment at the high temperature.

Fig. S15 HAADF-STEM-EDS mapping images of $\text{Fe}_{\text{Fe-O-Fe}}$ -UP/CA catalysts.

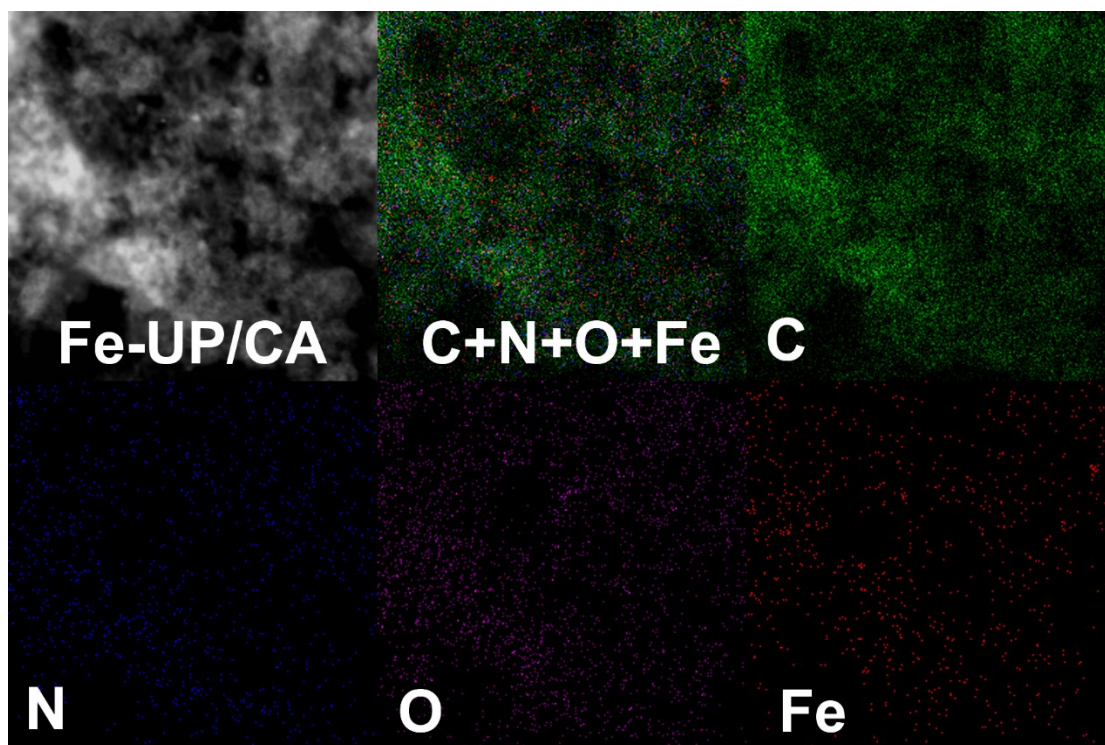


Fig. S16 One typical TEM image of Fe_{Fe-O-Fe}-UP/CA catalysts (a), around 100 Fe_{Fe-O-Fe} UPs were counted and analyzed to plot the histogram (b). Note that a small portion of particles with sizes larger than 5 nm were not included in the histogram.

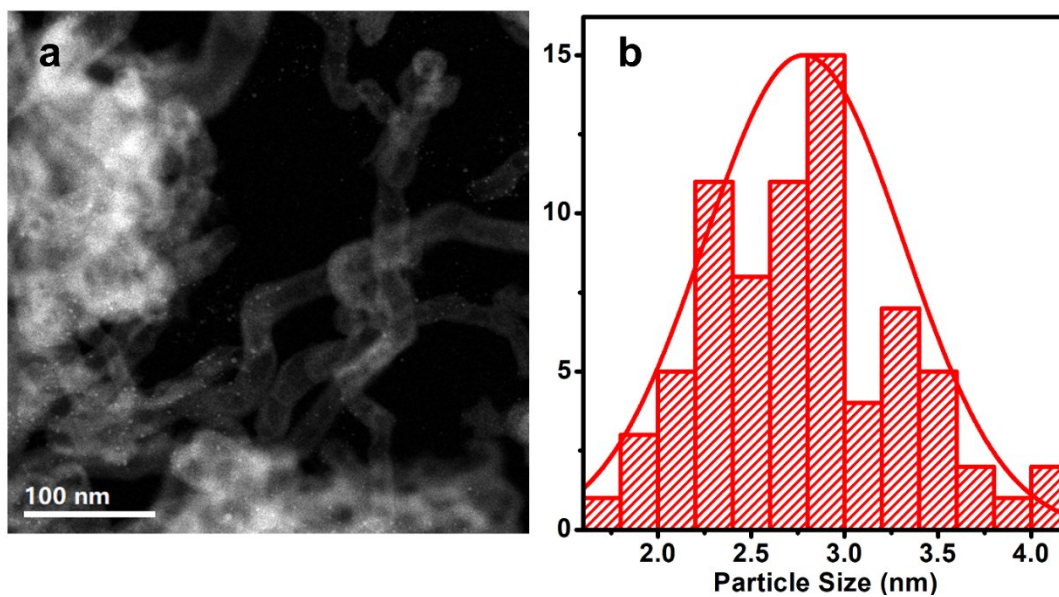


Fig. S17 The distributions of mesoporous pore diameter of Fe_{Fe-O-Fe}-UP/CA catalysts (a), Fe-SA/CA catalysts (b), C_{ZIF-TA} catalysts (c) and C_{ZIF} materials (d) based on the BJH method.

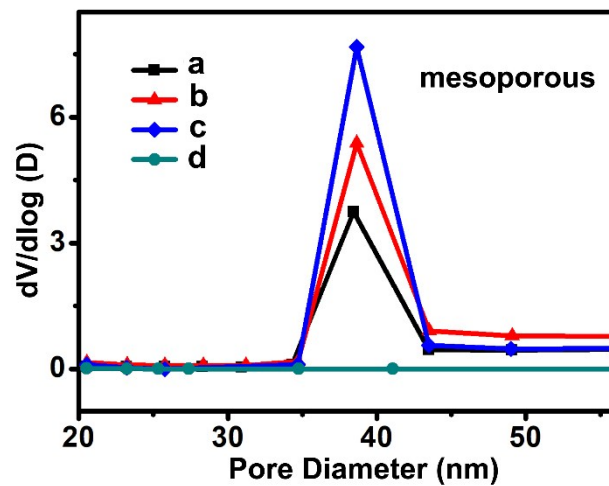


Fig. S18 The distributions of macropore pore diameter of Fe_{Fe-O-Fe}-UP/CA catalysts (a), Fe-SA/CA catalysts (b), C_{ZIF-TA} catalysts (c) and C_{ZIF} materials (d) based on the BJH method.

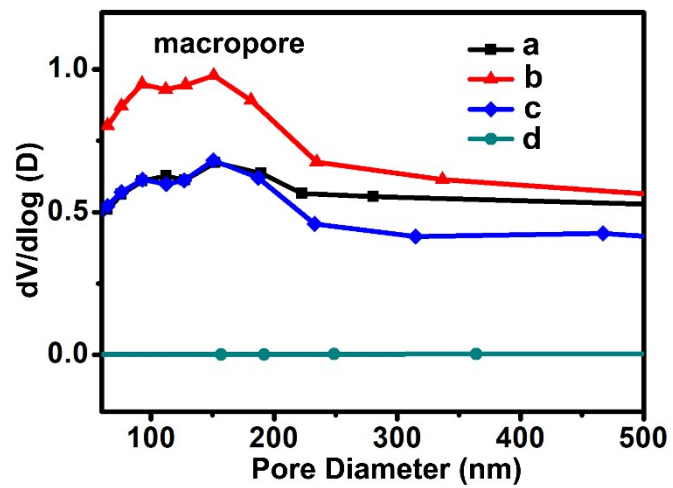


Fig. S19 High-resolution C 1s spectra of Fe_{Fe-O-Fe}-UP/CA catalysts.

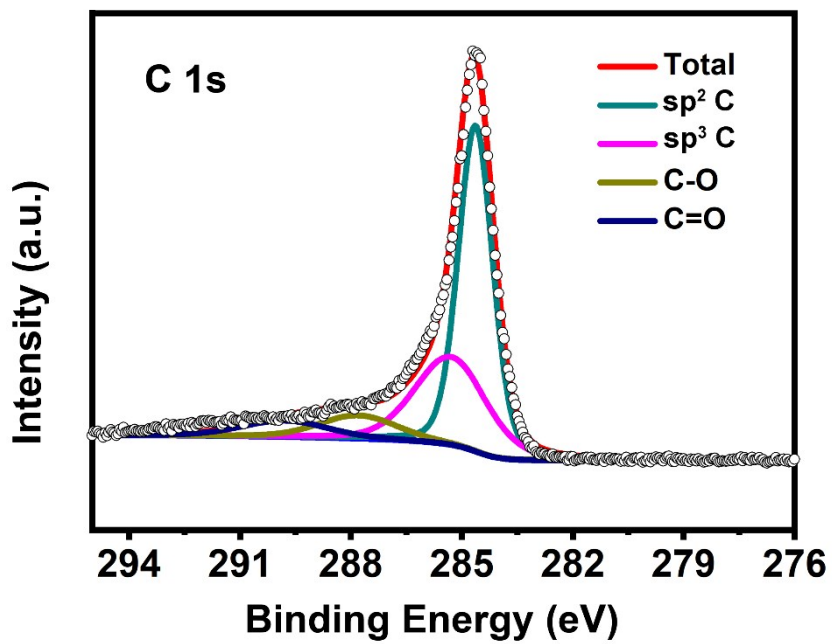


Fig. S20 High-resolution N 1s spectra of C_{ZIF-TA} catalysts.

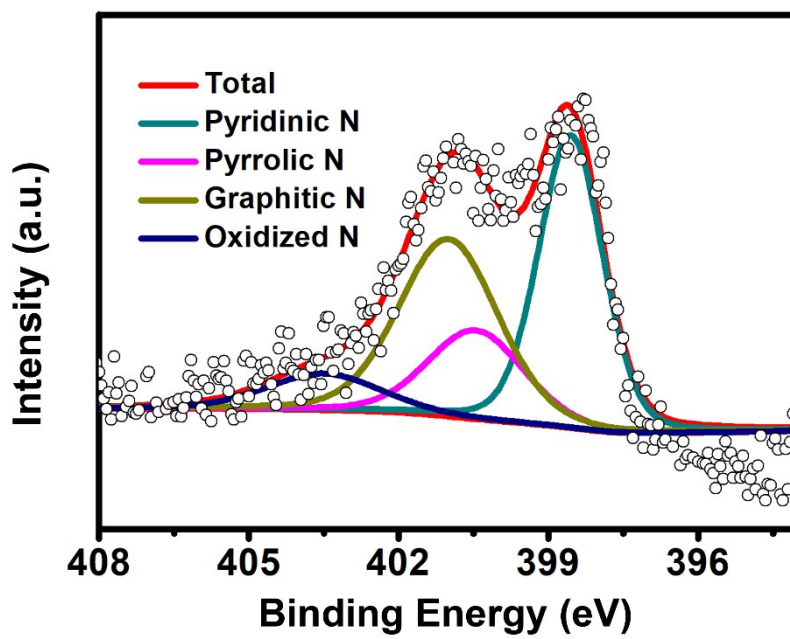


Fig. S21 The N contents of different types of N species of Fe_{Fe-O-Fe}-UP/CA catalysts (a) and C_{ZIF-TA} catalysts (b).

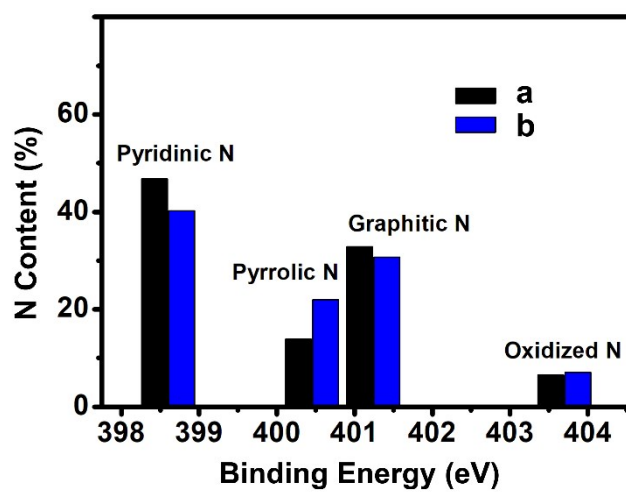


Fig. S22 Comparison in FT-EXAFS spectra between $\text{Fe}_{\text{Fe-O-Fe}}\text{-UP/CA}$ catalysts and other samples: (a) $\text{Fe}_{\text{Fe-O-Fe}}\text{-UP/CA}$ catalysts and Fe foil, (b) $\text{Fe}_{\text{Fe-O-Fe}}\text{-UP/CA}$ catalysts and FePc, (c) $\text{Fe}_{\text{Fe-O-Fe}}\text{-UP/CA}$ catalysts and Fe_2O_3 , (d) $\text{Fe}_{\text{Fe-O-Fe}}\text{-UP/CA}$ catalysts and Fe NPs, (e) $\text{Fe}_{\text{Fe-O-Fe}}\text{-UP/CA}$ catalysts and Fe-SA-NCs catalysts, and (f) $\text{Fe}_{\text{Fe-O-Fe}}\text{-UP/CA}$ catalysts and carbon materials containing Fe-O-Fe moiety. The FT-EXAFS spectrum of Fe-NC-SA catalyst was reported in our previous work ¹ and that of carbon materials containing Fe-O-Fe moiety was from the work recently reported by Xing group. ²

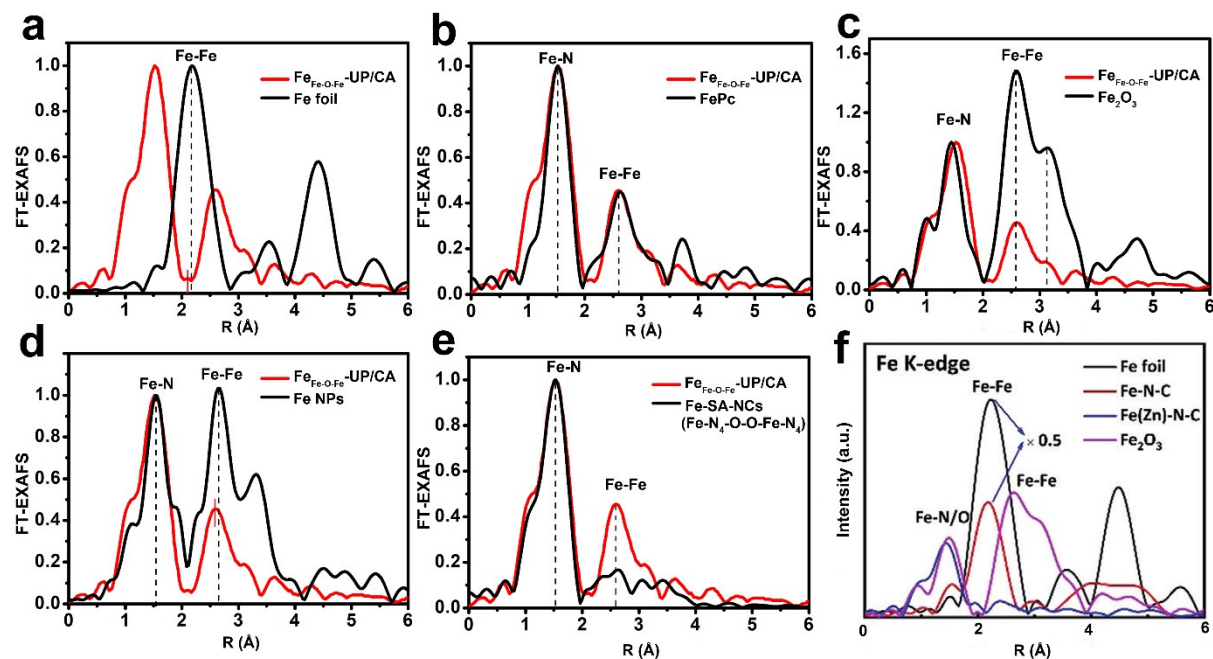
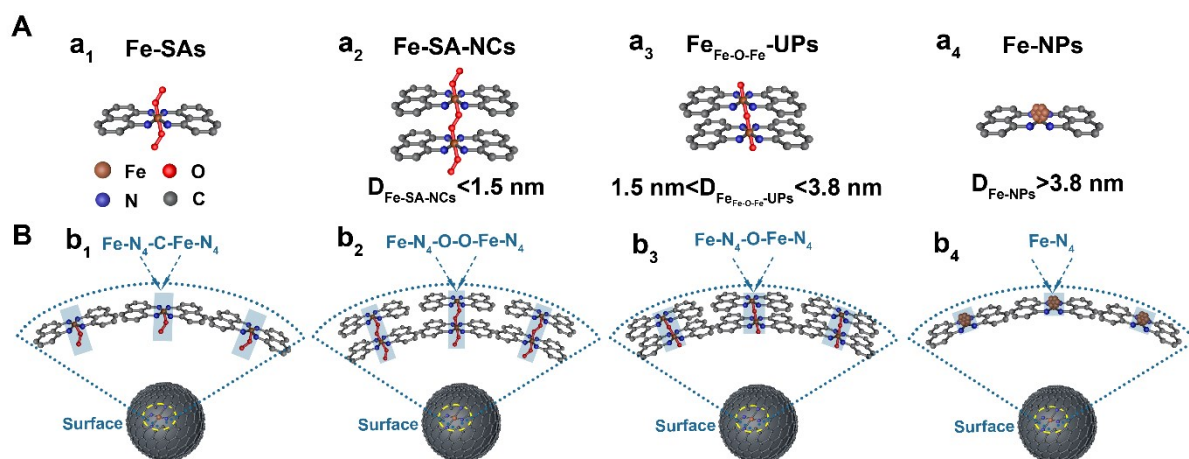


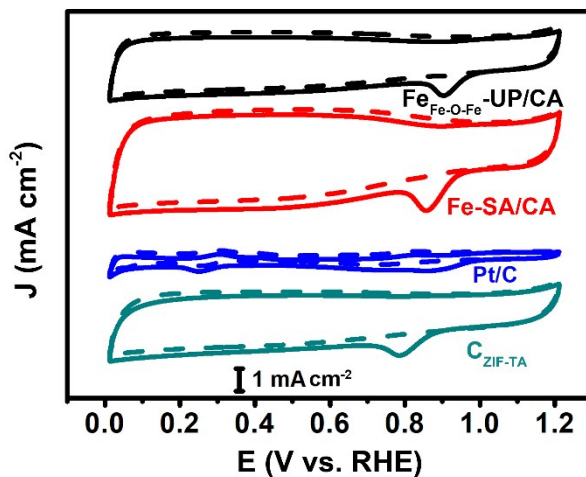
Fig. S23 (A) Models of the possible local atomic configuration around Fe atoms within carbon materials with the increasing particle size. (B) Schematic model of the local atomic configuration around Fe atoms in Fe-SA/CA catalysts (a_2), Fe-SA-NCs catalysts with sizes smaller than 1.5 nm (b_2), Fe_{Fe-O-Fe}-UP/CA catalysts with sizes between 1.5 nm and 3.8 nm (c_2) and Fe-NP/CA catalysts with sizes bigger than 3.8 nm (d_2).



In our previous work, the formation of Fe-N₄-O-O-Fe-N₄ moiety in our Fe-SA-NCs catalysts (Fig. S23B-b₂) is achieved by controlling the molar ratio of Fe-to-TA. In addition, the oxygen atoms in the Fe-N₄-O-Fe-N₄ moiety mainly result from TA.¹ With the increasing molar ratio of Fe-to-TA, the size of Fe-based particles would also increase (Fig. S23). And the ratio of oxygen atoms in the Fe-N₄-O-Fe-N₄ moiety become lower, which also result in the decrease in the distance between Fe-N₄ moiety in the Fe species (Fig. S23A-a₃).

In this work, Fe precursors are also complexed with oxygen atoms of TA molecules. Accordingly, oxygen atoms may also exist in the Fe-N₄ moiety as bridges after the pyrolysis. Since the size of Fe-UPs is between 1.5 and 3.8 nm (Fig. S23A-a₃), it is highly possible that oxygen atoms may also exist in the Fe-N₄-O-Fe-N₄ moiety as bridges. And Fe-UPs are composed of tens of Fe-N₄-O-Fe-N₄ moiety (Fig. S23B-b₃).

Fig. S24 CV curves of $\text{Fe}_{\text{Fe-O-Fe}}\text{-UP/CA}$ catalysts (black curve), Fe-SA/CA catalysts (red curve), the commercial Pt/C catalyst (blue curve) and $\text{C}_{\text{ZIF-TA}}$ catalysts (cyan curve) measured in 0.1 M KOH saturated with N_2 (dashed curves) or O_2 (solid curves).



As shown in Fig. S24, the potentials of the oxygen reduction peaks of $\text{C}_{\text{ZIF-TA}}$ catalysts, Fe-SA/CA catalysts, and $\text{Fe}_{\text{Fe-O-Fe}}\text{-UP/CA}$ catalysts are 0.79 V (vs RHE), 0.86 V (vs RHE) and 0.90 V (vs RHE), respectively. In addition, the potential of the oxygen reduction peaks of both Fe-SA/CA catalysts, and Fe-UP/CA catalysts are much higher than that (0.856 V vs RHE) of the commercial Pt/C catalyst.

Fig. S25 LSV curves of Fe-NP/CA catalysts (a) and Fe_{Fe-O-Fe}-UP/CA catalysts (b) measured in 0.1M KOH.

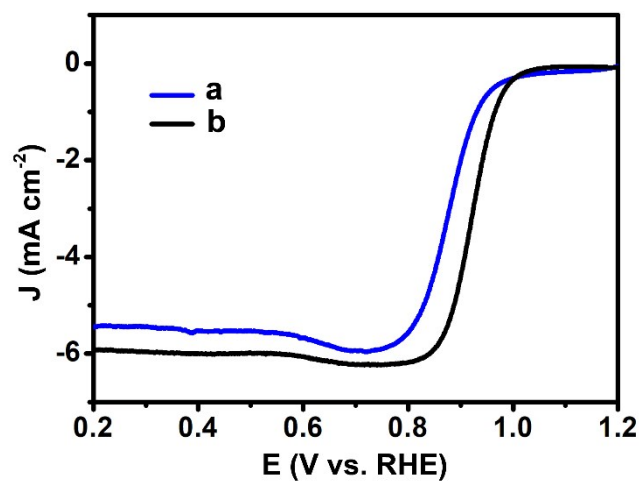


Fig. S26 LSV curves of Fe_{Fe-O-Fe}-UP/CA catalysts measured in O₂-saturated 0.1 M KOH at various rotation speeds.

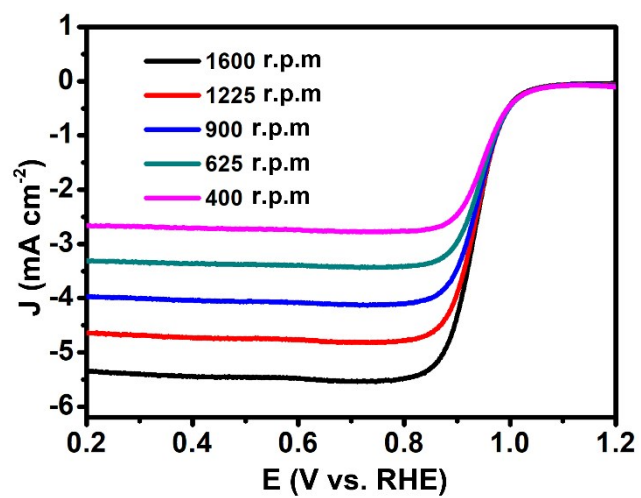


Fig. S27 (a) LSV curves of the commercial Pt/C catalyst measured in O₂-saturated 0.1 M KOH at various rotation speeds and (b) their K-L plots at different potentials.

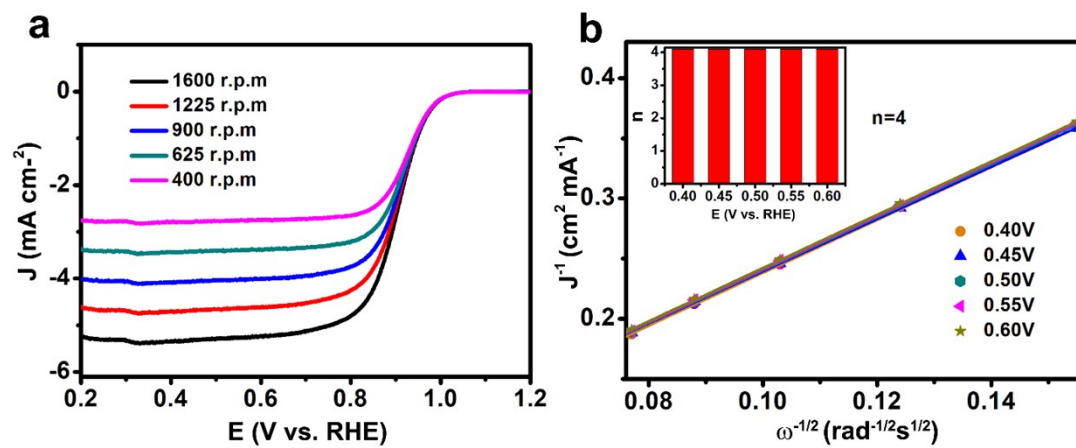


Fig. S28 (a) LSV curves of Fe-SA/CA catalysts measured in O₂-saturated 0.1 M KOH at various rotation speeds and (b) their K-L plots at different potentials.

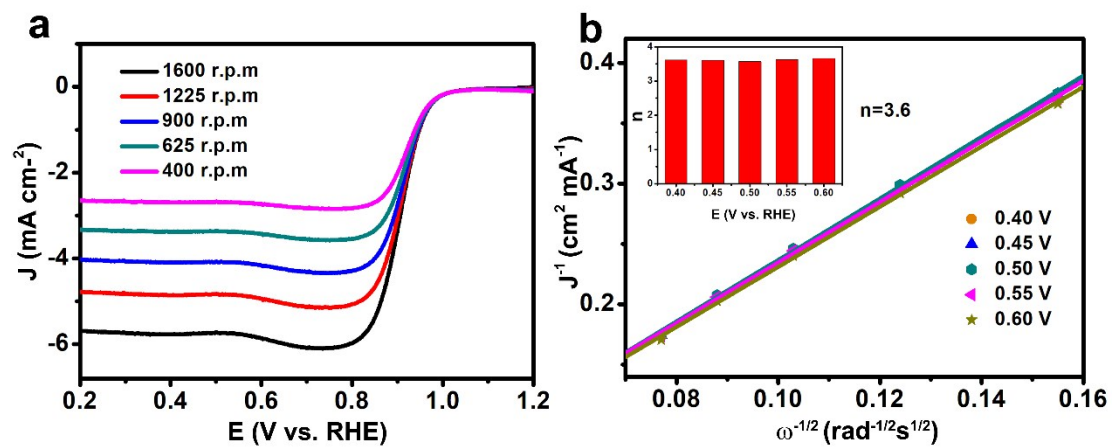


Fig. S29 (a) LSV curves of C_{ZIF-TA} catalysts measured in O_2 -saturated 0.1 M KOH at various rotation speeds and (b) their K-L plots at different potentials.

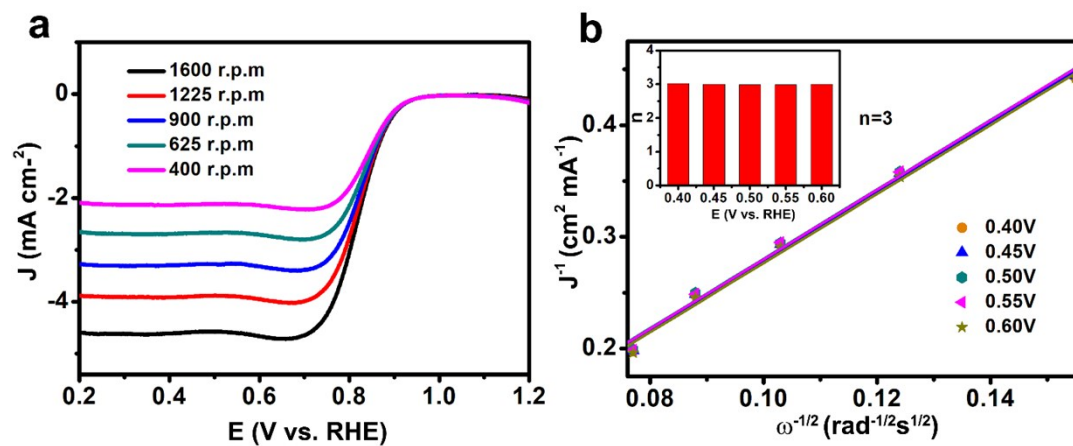


Fig. S30 ORR LSV curves of the commercial Pt/C catalyst before and after 5000 cycles in O₂-saturated 0.1 M KOH.

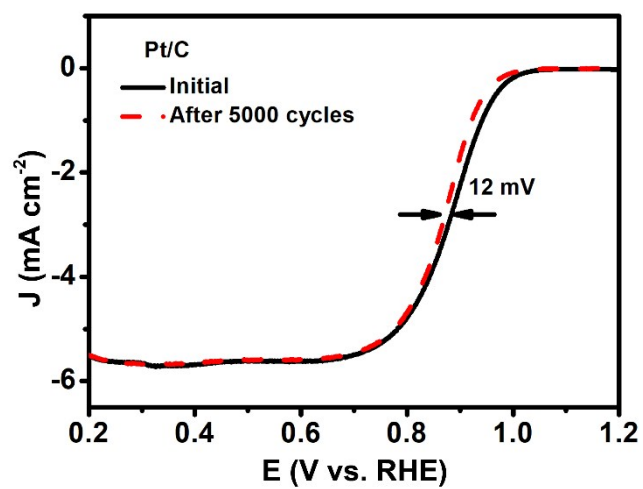


Fig. S31 Open-circuit plot of the primary Zn-air battery assembled by Fe-NP/CA catalysts.

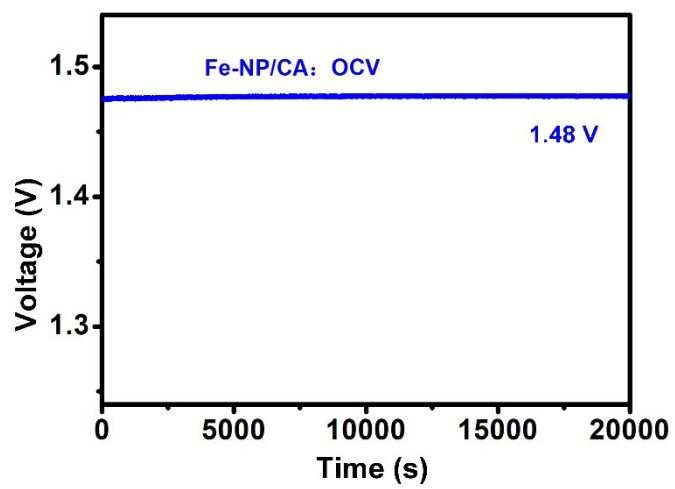


Fig. S32 Discharge polarization curve and the corresponding power density curve of the primary Zn-air battery assembled by Fe-NP/CA catalysts.

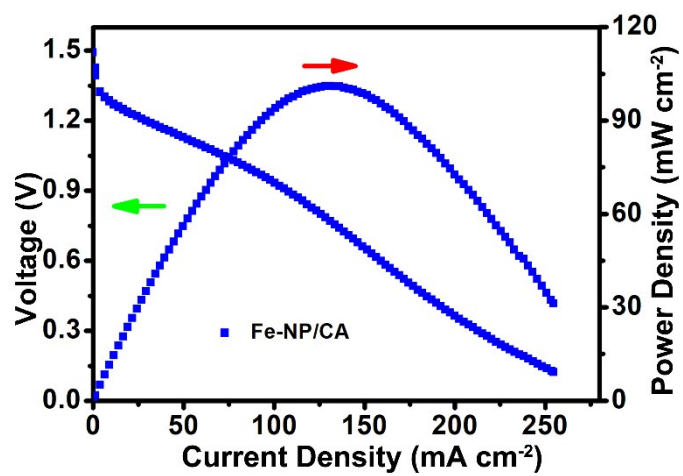


Fig. S33 Specific capacity at a current density of 100 mA cm^{-2} of Fe-NP/CA catalysts based primary Zn-air battery.

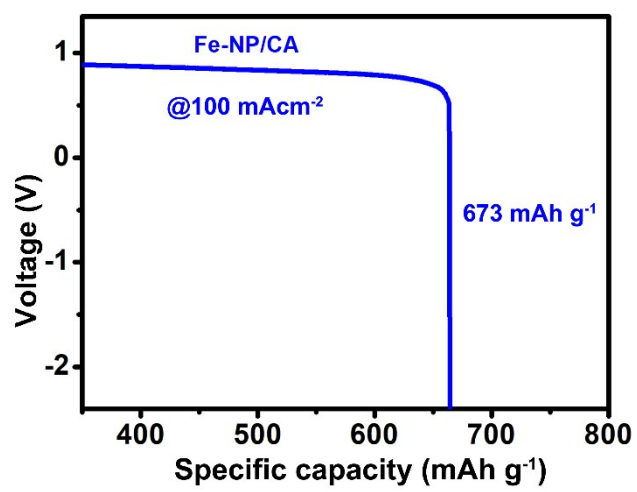


Fig. S34 Galvanostatic discharge curve of the primary Zn-air battery assembled by Fe-NP/CA catalysts at different current densities.

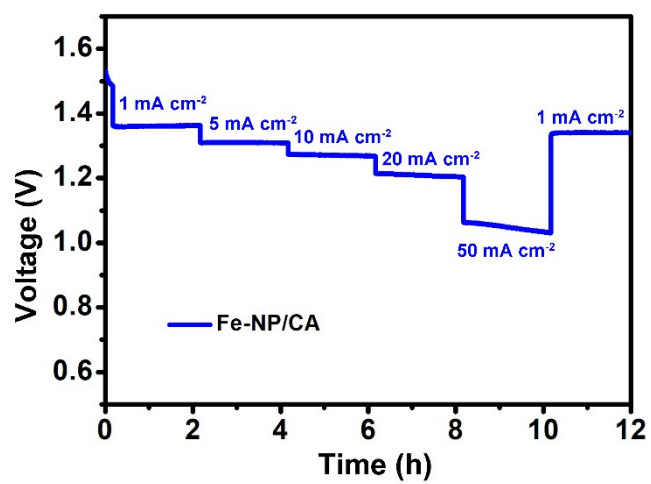


Fig. S35 Long-time discharge curve of the primary Zn-air battery assembled by Fe-NP/CA catalysts at the current density of 20 mA cm⁻².

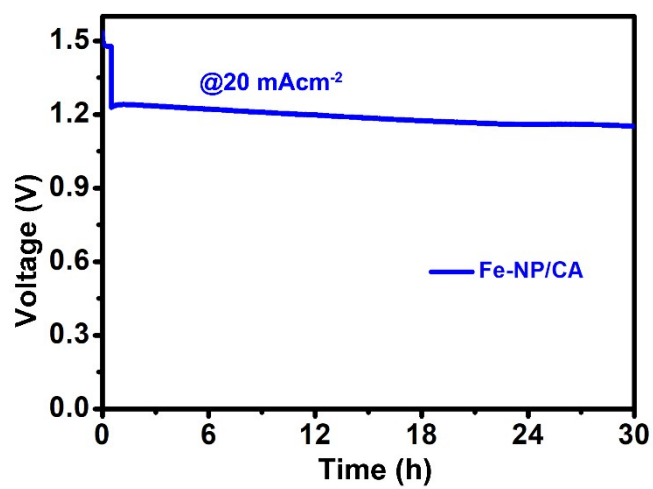


Table S1. Summarized I_D/I_G values of C_{ZIF} materials, C_{ZIF-TA} catalysts, Fe-SA/CA catalysts and $Fe_{Fe-O-Fe}$ -UP/CA catalysts.

Catalysts	I_D/I_G
C_{ZIF} materials	1.44
C_{ZIF-TA} catalysts	1.12
Fe-SA/CA catalysts	1.10
$Fe_{Fe-O-Fe}$ -UP/CA catalysts	0.91

Table S2. Summarized BET surface area and pore volumes of C_{ZIF} materials, C_{ZIF-TA} catalysts, Fe-SA/CA catalysts and Fe_{Fe-O-Fe}-UP/CA catalysts.

Catalysts	BET Surface Area (m ³ g ⁻¹)	Pore Volume (cm ³ g ⁻¹)
C _{ZIF} materials	69.7	0.04
C _{ZIF-TA} catalysts	957.3	1.28
Fe-SA/CA catalysts	916.8	1.46
Fe _{Fe-O-Fe} -UP/CA catalysts	628.8	1.08

Table S3. Relative contents (at. %) of different C species determined from the deconvoluted peaks for C1s.

Samples	sp ² C (at.%)	sp ³ C (at.%)	C-O (at.%)	C=O (at.%)
Fe _{Fe-O-Fe} -UP/CA catalysts	59.54	20.87	10.75	8.83

Table S4. Summarized contents of different types of N species in C_{ZIF-TA} catalysts and Fe_{Fe-O-Fe}-UP/CA catalysts.

N (eV)	C _{ZIF-TA} catalysts (at.%)	Fe _{Fe-O-Fe} -UP/CA catalysts (at.%)
Pyridinic N (398.6)	40.21	46.75
Pyrrolic N (400.45)	22	13.89
Graphitic N (401.24)	30.74	32.84
Oxidized N (403.7)	7.07	6.51

Table S5. Summarized data of C_{ZIF-TA} catalysts, C_{ZIF-Fe} catalysts, Fe-SA/CA catalysts, Fe-NP/CA catalysts, Fe_{Fe-O-Fe}-UP/CA catalysts and the commercial Pt/C catalyst towards ORR.

Samples	Onset potential (V vs. RHE)	Half potential (V vs. RHE)	Current density at 0.2 V (mA cm ⁻²)
C _{ZIF-TA} materials	0.94	0.82	4.59
C _{ZIF-Fe} catalysts	1.02	0.91	5.54
Fe _{Fe-O-Fe} -UP/CA catalysts	1.08	0.93	5.76
Fe-SA/CA catalysts	1.03	0.90	5.68
Fe-NP/CA catalysts	1.02	0.90	5.26
the commercial Pt/C catalyst	1.00	0.89	5.53

Table S6. Comparison in E_{onset} and $E_{1/2}$ of Fe-N-C catalysts reported in literature and Fe_{Fe-O-Fe}-UP/CA catalysts in this work toward ORR in alkaline medium.

Catalysts	$E_{1/2}$ Vs RHE	E_{onset} Vs RHE	Ref.
Fe-N-C/SAC	0.84	0.95	<i>Nano Energy</i> , 2020, 72, 104670. ³
Fe ₃ O ₄ @Fe-N-C	0.89	1.007	<i>Carbon</i> , 2020, 162, 245-255. ⁴
Fe-N-C/MXene	0.84	0.92	<i>ACS Nano</i> , 2020, 14 (2), 2436-2444. ⁵
Fe-SAs-N/C-20	0.909	-	<i>J. Am. Chem. Soc.</i> , 2018, 140 (37), 11594-11598. ⁶
FeNx-C-N/g-GEL	0.9	1.0	<i>J. Mater. Chem. A</i> , 2019, 7 (44), 25557-25566. ⁷
Fe-N-C SAC	0.88	-	<i>J. Mater. Chem. A</i> , 2020, 8 (19), 9981-9990. ⁸
3DOM Fe-N-C-900	0.875	-	<i>Nano Energy</i> , 2020, 71, 104547. ⁹
Fe SAs/N-C	0.91	-	<i>ACS Catal.</i> , 2019, 9 (3), 2158-2163. ¹⁰
Fe-NSDC	0.84	0.96	<i>Small</i> , 2019, 15 (24), 1900307. ¹¹
Fe SAs/MC(950)	0.902	1.03	<i>ACS Energy Lett.</i> , 2018, 3 (10), 2383-2389. ¹²
MA-Fe-N/CNT	0.92	-	<i>J. Mater. Chem. A</i> , 2020, 8, 18891-18902 ¹³
N, S co-doped C _{PANI-TA-Fe} Fe-SA-NCs catalysts	0.923	1.09	<i>J. Mater. Chem. A</i> , 2020, 8, 17136-17149 ¹
Fe _{Fe-O-Fe} -UP/CA catalysts	0.93	1.08	This work

Table S7. Comparison of the power density of Zinc-air batteries assembled by nonprecious catalysts with recently reported results.

	Catalysts	Maximum power density (mW cm ⁻²)	R _(Catalyst:Pt/C)	Ref.
Fe-based Bimetallic Catalysts	NCAG/FeCo	117	1.3	14
	Pt/C-RuO ₂	92		
	PB@Met-700	148	1.1	15
	Pt/C+RuO ₂	138.9		
	FeCo-C/N	397.25	3	16
	Pt/C	131.54		
	Fe-NiNC-50	220	1.4	17
	Pt/C+Ir/C	160		
	Ni ₂ Fe ₁ @PANI-KOH900	256	1.3	18
	Pt/C+RuO ₂	192		
Fe Single-Atom Catalysts	Fe-N ₄ SAs/NPC	232	4.4	19
	Pt/C+Ir/C	52.8		
	Fe/N/S-CNTs	111	1.5	20
	Pt/C	73		
	Fe@CNG/NCNTs	101.3	1	21
	Pt/C+Ir/C	101.9		
	Fe-N/C-1/30	121.8	0.9	22
	Pt/C	132		
	Fe-NC SAC	180	1.5	8
	Pt/C-RuO ₂	120		
	SA-Fe-NHPC	266.4	1.7	23
	Pt/C	154.1		
	FeNCF	145	1.5	24
Pt/C	98			
3DOM Fe-N-C-900	235	1.2	9	
Pt/C	192			
	Fe _{Fe-O-Fe} -UP/CA catalysts	140.1	1.5	This work
	Pt/C	93.7		

References

- 1 H. Li, K. Du, C. Xiang, P. An, X. Shu, Y. Dang, C. Wu, J. Wang, W. Du, J. Zhang, S. Li, H. Tian, S. Wang and H. Xia, *J. Mater. Chem. A*, 2020, **8**, 17136-17149.
- 2 L. Gong, H. Zhang, Y. Wang, E. Luo, K. Li, L. Gao, Y. Wang, Z. Wu, Z. Jin, J. Ge, Z. Jiang, C. Liu and W. Xing, *Angew. Chem., Int. Ed.*, 2020, **59**, 13923-13928.
- 3 J. Hu, D. Wu, C. Zhu, C. Hao, C. Xin, J. Zhang, J. Guo, N. Li, G. Zhang and Y. Shi, *Nano Energy*, 2020, **72**, 104670.
- 4 S. Hu, W. Ni, D. Yang, C. Ma, J. Zhang, J. Duan, Y. Gao and S. Zhang, *Carbon*, 2020, **162**, 245-255.
- 5 L. Jiang, J. Duan, J. Zhu, S. Chen and M. Antonietti, *ACS Nano*, 2020, **14**, 2436-2444.
- 6 R. Jiang, L. Li, T. Sheng, G. Hu, Y. Chen and L. Wang, *J. Am. Chem. Soc.*, 2018, **140**, 11594-11598.
- 7 M. Hong, J. Nie, X. Zhang, P. Zhang, Q. Meng, J. Huang, Z. Xu, C. Du and J. Chen, *J. Mater. Chem. A*, 2019, **7**, 25557-25566.
- 8 C. Du, Y. Gao, J. Wang and W. Chen, *J. Mater. Chem. A*, 2020, **8**, 9981-9990.
- 9 X. Zhang, X. Han, Z. Jiang, J. Xu, L. Chen, Y. Xue, A. Nie, Z. Xie, Q. Kuang and L. Zheng, *Nano Energy*, 2020, **71**, 104547.
- 10 Z. Yang, Y. Wang, M. Zhu, Z. Li, W. Chen, W. Wei, T. Yuan, Y. Qu, Q. Xu, C. Zhao, X. Wang, P. Li, Y. Li, Y. Wu and Y. Li, *ACS Catal.*, 2019, **9**, 2158-2163.
- 11 J. Zhang, M. Zhang, Y. Zeng, J. Chen, L. Qiu, H. Zhou, C. Sun, Y. Yu, C. Zhu and Z. Zhu, *Small*, 2019, **15**, 1900307.
- 12 Z. K. Yang, C.-Z. Yuan and A.-W. Xu, *ACS Energy Lett.* 2018, **3**, 2383-2389.
- 13 W. Y. Noh, E. M. Kim, K. Y. Kim, J. H. Kim, H. Y. Jeong, P. Sharma, G. Lee, J.-W. Jang, S. H. Joo and J. S. Lee, *J. Mater. Chem. A*, 2020, **8**, 18891-18902.
- 14 Y. Chen, S. Hu, F. Nichols, F. Bridges, S. Kan, T. He, Y. Zhang and S. Chen, *J. Mater. Chem. A*, 2020, **8**, 11649-11655.
- 15 Y. Lian, K. Shi, H. Yang, H. Sun, P. Qi, J. Ye, W. Wu, Z. Deng and Y. Peng, *Small*, 2020, **16**, 1907368.
- 16 C. Zhang, H. Yang, D. Zhong, Y. Xu, Y. Wang, Q. Yuan, Z. Liang, B. Wang, W. Zhang, H. Zheng, T. Cheng and R. Cao, *J. Mater. Chem. A*, 2020, **8**, 9536-9544.
- 17 X. Zhu, D. Zhang, C.-J. Chen, Q. Zhang, R.-S. Liu, Z. Xia, L. Dai, R. Amal and X. Lu, *Nano Energy*, 2020, **71**, 104597.
- 18 J. Zhang, M. Zhang, L. Qiu, Y. Zeng, J. Chen, C. Zhu, Y. Yu and Z. Zhu, *J. Mater. Chem. A*, 2019, **7**, 19045-19059.
- 19 Y. Pan, S. Liu, K. Sun, X. Chen, B. Wang, K. Wu, X. Cao, W.-C. Cheong, R. Shen, A. Han, Z. Chen, L. Zheng, J. Luo, Y. Lin, Y. Liu, D. Wang, Q. Peng, Q. Zhang, C. Chen and Y. Li, *Angew. Chem., Int. Ed.*, 2018, **57**, 8614-8618.
- 20 H. Jin, H. Zhou, W. Li, Z. Wang, J. Yang, Y. Xiong, D. He, L. Chen and S. Mu, *J. Mater. Chem. A*, 2018, **6**, 20093-20099.
- 21 Q. Wang, Y. Lei, Z. Chen, N. Wu, Y. Wang, B. Wang and Y. Wang, *J. Mater. Chem. A*, 2018, **6**, 516-526.
- 22 W. Wei, X. Shi, P. Gao, S. Wang, W. Hu, X. Zhao, Y. Ni, X. Xu, Y. Xu, W. Yan, H. Ji and M. Cao, *Nano Energy*, 2018, **52**, 29-37.
- 23 G. Chen, P. Liu, Z. Liao, F. Sun, Y. He, H. Zhong, T. Zhang, E. Zschech, M. Chen, G. Wu, J. Zhang and X. Feng, *Adv. Mater.*, 2020, **32**, 1907399.
- 24 J. Zhang, Y. Liu, Z. Yu, M. Huang, C. Wu, C. Jin and L. Guan, *J. Mater. Chem. A*, 2019, **7**, 23182-23190.